



Proof-of-concept studies with a computationally designed M^{pro} inhibitor as a synergistic combination regimen alternative to Paxlovid

Christina Papini^{a,1} , Irfan Ullah^{b,1} , Amalendu P. Ranjan^c , Shuo Zhang^d, Qihao Wu^e , Krasimir A. Spasov^a , Chunhui Zhang^e , Walther Mothes^d , Jason M. Crawford^e , Brett D. Lindenbach^d, Pradeep D. Uchil^d , Priti Kumar^{b,2} , William L. Jorgensen^{e,2} , and Karen S. Anderson^{a,f,2}

Contributed by William L. Jorgensen; received November 24, 2023; accepted February 27, 2024; reviewed by Daria Hazuda and Dennis C. Liotta

As the SARS-CoV-2 virus continues to spread and mutate, it remains important to focus not only on preventing spread through vaccination but also on treating infection with direct-acting antivirals (DAA). The approval of Paxlovid, a SARS-CoV-2 main protease (M^{pro}) DAA, has been significant for treatment of patients. A limitation of this DAA, however, is that the antiviral component, nirmatrelvir, is rapidly metabolized and requires inclusion of a CYP450 3A4 metabolic inhibitor, ritonavir, to boost levels of the active drug. Serious drug–drug interactions can occur with Paxlovid for patients who are also taking other medications metabolized by CYP4503A4, particularly transplant or otherwise immunocompromised patients who are most at risk for SARS-CoV-2 infection and the development of severe symptoms. Developing an alternative antiviral with improved pharmacological properties is critical for treatment of these patients. By using a computational and structure-guided approach, we were able to optimize a 100 to 250 μ M screening hit to a potent nanomolar inhibitor and lead compound, Mpro61. In this study, we further evaluate Mpro61 as a lead compound, starting with examination of its mode of binding to SARS-CoV-2 M^{pro}. In vitro pharmacological profiling established a lack of off-target effects, particularly CYP450 3A4 inhibition, as well as potential for synergy with the currently approved alternate antiviral, molnupiravir. Development and subsequent testing of a capsule formulation for oral dosing of Mpro61 in B6-K18-hACE2 mice demonstrated favorable pharmacological properties, efficacy, and synergy with molnupiravir, and complete recovery from subsequent challenge by SARS-CoV-2, establishing Mpro61 as a promising potential preclinical candidate.

SARS-CoV-2 | protease inhibitor | Mpro61 | drug synergy | molnupiravir

After 4 y of precautions, “COVID fatigue” has left many institutions and individuals believing that the risk of SARS-CoV-2 infection is no longer high and that the virus is simply another “seasonal flu.” However, new variants are continuing to emerge, and cases continue to peak around holidays and after large gatherings (1–3). Even with widespread vaccination, hospitalizations and deaths due to COVID are significantly higher than for the flu (2). As the spread and evolution of SARS-CoV-2 continues, it is important to treat COVID as a serious disease and to continue to not only work to prevent transmission but to develop improved antiviral treatments as well. In the development of novel antivirals, the SARS-CoV-2 main protease (M^{pro}) has been established as a prominent drugable target (4–6). Coronavirus proteases were well studied as antiviral targets following the initial SARS outbreak, and M^{pro} in particular is highly conserved, with a recognition site distinct from that of human cysteine proteases (5–8). These factors have made M^{pro} the target for a number of antiviral efforts (7–14).

Recently, Paxlovid (Pfizer) became the first and currently only FDA-approved SARS-CoV-2 therapy targeting M^{pro} (15–17). Paxlovid is a combination therapy consisting of nirmatrelvir, the antiviral component, along with the HIV drug ritonavir as a “booster” drug. While the peptidomimetic nirmatrelvir is highly potent and has high bioavailability, it is rapidly metabolized in vivo, necessitating the addition of a booster drug (15–18). Ritonavir has previously been formulated in combination with various drugs as a strong CYP450-3A4 inhibitor, making it a critical component of Paxlovid to slow the metabolism of nirmatrelvir and allow it to remain in circulation (18–21). However, the addition of a metabolic inhibitor can lead to major drug–drug interactions, which can be a problem for patients who are taking medications for other conditions, particularly immunocompromised patients who are more at risk for complications from COVID (22). These serious complications have already been observed in multiple cases where transplant patients were inadvertently prescribed Paxlovid without an appreciation for possible drug–drug interactions.

Significance

While Paxlovid has been instrumental in treating SARS-CoV-2 infections, the necessary co-formulation with a metabolic inhibitor does not guarantee safe administration and a well-tolerated drug profile for patients taking other medications, particularly the immunocompromised who are most at risk for severe disease. Our computational and structure-guided design has translated a weak virtual screening hit to a low-nM SARS-CoV-2 main protease inhibitor, Mpro61, which shows potent biochemical activity in vitro and antiviral efficacy in cells. Mpro61 shows few off-target effects and improved pharmacological properties and thus would not require metabolic inhibition. Mpro61 displays synergistic effects with the SARS-CoV-2 antiviral molnupiravir as an oral combination regimen in B6-K18-hACE2 mice, making it a promising candidate as a Paxlovid alternative.

Reviewers: D.H., Generate Biomedicines; and D.C.L., Emory University.

Competing interest statement: Yale University has filed a patent application covering Mpro61.

Copyright © 2024 the Author(s). Published by PNAS. This open access article is distributed under Creative Commons Attribution-NonCommercial-NoDerivatives License 4.0 (CC BY-NC-ND).

¹C.P. and I.U. contributed equally to this work.

²To whom correspondence may be addressed. Email: priti.kumar@yale.edu, william.jorgensen@yale.edu, or karen.anderson@yale.edu.

This article contains supporting information online at <https://www.pnas.org/lookup/suppl/doi:10.1073/pnas.2320713121/-DCSupplemental>.

Published April 15, 2024.

As a result, these patients were hospitalized shortly afterward not due to their COVID infections but rather due to a drug buildup of tacrolimus and renal toxicity (23, 24). The majority of transplant patients are on a therapeutic regimen that includes tacrolimus to prevent organ rejection. Tacrolimus has a narrow therapeutic index and is metabolized by liver CYP450-3A4, and other medications that are inhibitors should (or must) be avoided (22). Therefore, to avoid these complications with drug interactions, the nucleoside inhibitor, molnupiravir, is often prescribed to transplant patients diagnosed with COVID infections (25). New antivirals are desirable that have improved pharmacokinetic (PK) properties and which do not inhibit CYP450-3A4, allowing them to be given without metabolic inhibitors to decrease a risk of drug–drug interactions in vulnerable patients. Other M^{pro} inhibitors under development include ensitrelvir, although its effect on CYP450-3A4 has recently been reported (26, 27). There have also been recent efforts to improve the metabolic stability of known M^{pro} inhibitors (28).

In previous publications, we have described strategies for the computational and structural design of novel COVID antivirals (12–14). In these studies, an approximately 2,000 compound FDA-approved drug library was virtually screened to identify 14 inhibitors of the SARS-CoV-2 main protease (12). Of these hit compounds, the antiepileptic drug perampanel (Fig. 1), having an IC_{50} value in the 100 to 250 μM range, was chosen for optimization using a combination of computer-aided design as well as biochemical, cellular, and structural studies (13, 14). The pathway utilized for free energy perturbation (FEP) guided lead optimization is illustrated in Fig. 1 that highlights several key

enhancements that improved potency. Based upon the FEP guidance, a positional change of the two-carbonyl in the pyridinone ring to the six-position, swapping the positions of benzene and pyridine rings attached to the pyridinone ring, and addition of a chlorine in the meta position of the benzene ring resulted in a 10-fold improvement in potency (Mpro6). Modification of this compound by replacement of the cyanophenyl group with a uracil (Mpro8) revealed a small increase in potency. Further elaboration of the scaffold by addition of substituents to build into the S4 subsite of the binding pocket of the active site led to significantly enhanced potency in the nanomolar range, $IC_{50} = 120$ nM and 28 nM, respectively, with the addition of a smaller propyl group (Mpro24) and larger phenyl group off the meta position of the benzyl ring (Mpro43). While Mpro43 showed low micromolar antiviral efficacy in cellular assays, the addition of a methyl group to the uracil ring (Mpro61) significantly enhanced cell permeability to achieve nanomolar potency ($EC_{50} = 80$ nM) (13, 14). After preparation of several dozen compounds, Mpro61 was developed and identified as a promising lead compound due to its inhibitory activity in biochemical assays and its inhibition of replication in cellular assays (13, 14).

In the current study, we further evaluate Mpro61 as a lead compound and preclinical candidate, utilizing structural studies to examine the binding of Mpro61 by M^{pro} , in vitro pharmacological profiling to examine possible off-target effects and toxicity, cellular studies to examine synergy of Mpro61 with the FDA-approved RNA-dependent RNA polymerase (RdRp) inhibitor molnupiravir, and in vivo studies in mice examining levels of

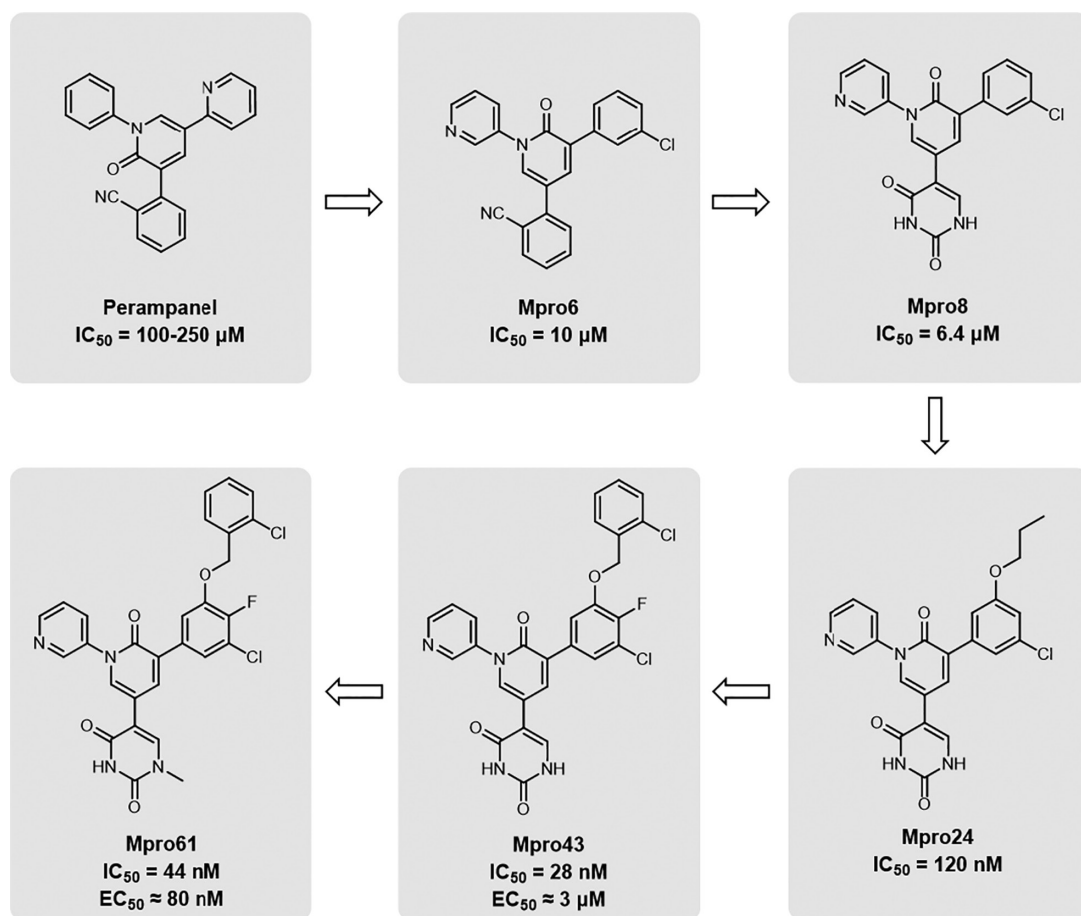


Fig. 1. Computational and structure-guided optimization of the docking hit compound, perampanel. The representative optimization steps shown here highlight reorganization of the scaffold rings (Mpro6), modification to a uracil group (Mpro8), oxyalkyl extension into additional subsites to achieve submicromolar inhibition (Mpro24 and Mpro43), and methylation of the uracil group to improve potency in cells (Mpro61). IC_{50} and EC_{50} values were previously published (12–14).

Mpro61 in serum and tissue as well as efficacy and synergy with molnupiravir in a mouse model of SARS-CoV-2 infection.

Results

A series of structural, biochemical, cellular, and in vivo experiments were carried out to further evaluate Mpro61 as a preclinical lead candidate. These studies included defining the mode of binding through structural studies, evaluation of possible off-target effects, and additional cellular studies using a replicon assay to examine possible synergy with an RdRp inhibitor. This effort also included in vivo studies to assess PK properties and antiviral efficacy in the B6-K18-hACE2 mouse model with infectious SARS-CoV-2 virus with a bioluminescent reporter that allows real-time imaging of viral infection (29, 30).

X-ray Crystallography Studies. The mode of binding for Mpro61 to M^{pro} was investigated through X-ray crystallography. Crystallization of the compound in complex with M^{pro} yielded a 2.3 Å structure (Fig. 2). The overall binding mode was in line with that seen for previously published peramppanel derivatives, with the three-pyridyl group blocking the catalytic dyad (Cys145 and His41) in the S1 subsite, the methyluracil ring residing in the S1' subsite, the chlorofluorophenyl group in the S2 subsite, and the chlorophenyl group extending into the S3-S4 subsites. Within the active site, Mpro61 forms an extensive hydrogen bonding network. This network consists of six hydrogen bonds: between the pyridinone carbonyl oxygen and the backbone nitrogen of E166 (3.0 Å), between the oxyalkyl oxygen and the sidechain nitrogen of Q189 (3.2 Å), between the pyridine nitrogen and the sidechain nitrogen of H163 (2.8 Å), and a series of bonds between the oxygen–nitrogen–oxygen uracil edge and the backbone nitrogen of G143 (2.8 Å), the backbone oxygen of T26 (3.3 Å), and the backbone nitrogen of T26 (3.0 Å).

In Vitro Pharmacological Profiling to Assess Off-Target Effects. Following structural evaluation of Mpro61, we wanted to look at any off-target effects that may occur in vivo when dosing

with Mpro61 or other lead compounds, Mpro48 and Mpro57. Our previous studies have shown these compounds to be potent inhibitors of M^{pro} in biochemical and antiviral assays and a lack of general cellular cytotoxicity ($CC_{50} > 100 \mu M$) (13, 14). These compounds were evaluated by in vitro pharmacological profiling against a panel of 33 targets composed of a range of prominent CYP450 isoforms, ion channels, and receptors (Fig. 3). Although Mpro48 showed significant inhibition of the hERG ion channel as well as inhibition of some minor CYP450 isoforms, both Mpro57 and Mpro61 showed only slight inhibition of the hERG ion channel at a high concentration (10 μM), and no other significant off-target effects. While Mpro57 and Mpro61 were both viable candidates in terms of biochemical and cellular antiviral potency, cellular cytotoxicity, and a lack of off-target effects, given the stronger inhibition by Mpro61 over Mpro57 as reported previously, Mpro61 was chosen as the most promising candidate for further studies (13, 14).

Cellular Synergy Studies. Concurrently, we were interested in the potential synergy of Mpro61 with other SARS-CoV-2 antivirals, as combination therapies have proven to be effective treatments for other viral infections such as HIV, hepatitis C virus, and influenza virus, by inhibiting viral replication while avoiding mutant viruses and drug resistance (31). In choosing candidate antivirals to examine for synergy with Mpro61, we were particularly interested in compounds that did not affect metabolism by CYP450, and which inhibited a target other than M^{pro} . To this end, molnupiravir, an FDA-approved RdRp inhibitor, was chosen for synergy studies. Using the previously described SARS-CoV-2 replicon virus, inhibition of viral replication was tested using Mpro61 in combination with molnupiravir using a similar range of concentrations for each compound as employed in our previous assays (13, 14, 32). As illustrated in Fig. 4, the combination inhibitory data were analyzed using MacSynergy II (33), a 3D model for statistical evaluation of the combination assay. The resulting surface plots of the data reflect the difference between the experimental dose–response surface and the predicted additive surface. On a 3D model, a simple additive effect will

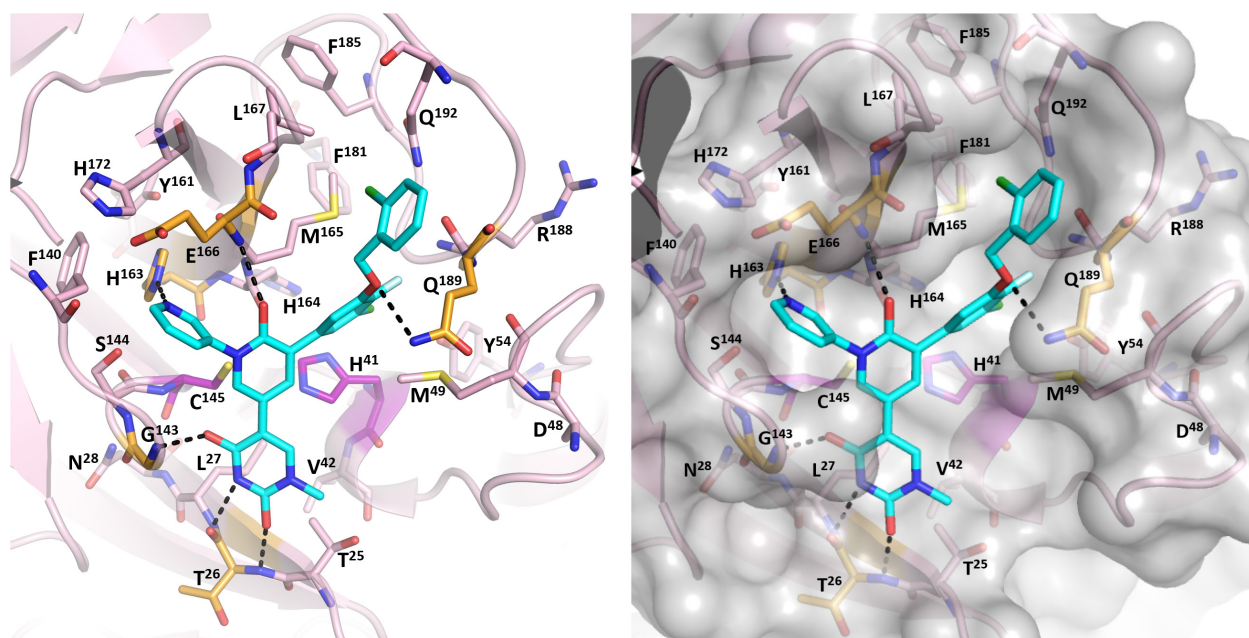


Fig. 2. Crystal structure of compound Mpro61 bound by the SARS-CoV-2 main protease (2.3 Å, PDB ID: 8UR9). Carbon atoms of Mpro61 are shown in cyan, carbon atoms of the catalytic dyad (C145 and H41) are shown in purple, and carbon atoms of residues involved in hydrogen bonding with Mpro61 are shown in orange. Hydrogen bonds are shown as dashed lines. The surface view (*Right*) shows the fit of Mpro61 within the active site.

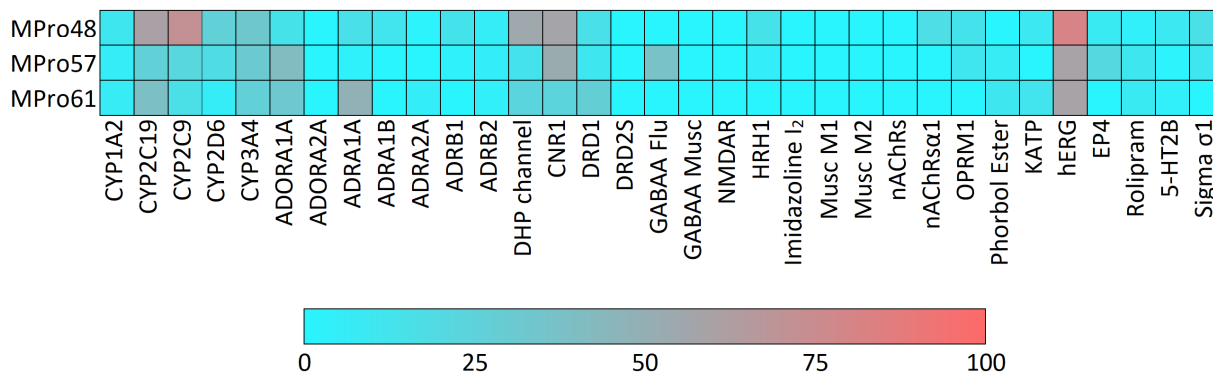


Fig. 3. Panel of 33 targets including CYP450 isoforms, ions channels, and receptors examined for off-target effects. Color-coding shows the percentage inhibition of each target in the presence of 10 μ M inhibitor. Mpro61 showed no significant off-target effects except slight inhibition of hERG ion channel at high concentrations.

result in a horizontal plane at 0% inhibition, whereas a synergistic agonistic or antagonistic effect will render a peak or depression above or below the horizontal plane. The surface plots generated for each combination showed that the percentage of inhibition was above the horizontal plane, which is indicative of a synergistic effect. The data from MacSynergy II analyses reveal that synergistic interactions were observed within the concentration ranges examined for antiviral efficacy between Mpro61 and molnupiravir. These observations served as a guide for the in vivo preclinical studies described below.

In Vivo Efficacy Studies in B6-K18hACE2 Mice. For in vivo experiments, we utilized the B6-K18-hACE2 mouse model, which is highly sensitive to infection with SARS-CoV-2 and displays acute lung infection, cytokine storm, as well as aggressive neuroinvasion of virus resulting in impaired respiratory function and mortality within a week of infection (34). Thus, antiviral interventions that are effective in preventing mortality in this mouse model are expected to be potent inhibitors of SARS-CoV-2 in a physiological setting. We employed a SARS-CoV-2 virus encoding a nanoluciferase reporter that allows for noninvasive detection by bioluminescence imaging (BLI) and tracking of viral spread and pathogenesis (29). The limited solubility of the free base form of Mpro61 made it challenging to formulate the drug

in suitable aqueous-based dosing solution for in vivo studies. To circumvent the requirement for the use of organic solvents like DMSO in in vivo studies, and improve aqueous solubility, a hydrochloride salt of Mpro61 was synthesized (*SI Appendix*). Using this hydrochloride salt form of Mpro61, we were able to prepare Mpro61-HCl in 5% Tween 80 in phosphate-buffered saline that could be administered at a 15 mg/kg dose via oral gavage in pilot experiments for a preliminary analysis of PK and antiviral efficacy. PK analyses were able to detect trace amounts of Mpro61-HCl in serum and some tissues of mice at 24 h after administration of a single oral dose, although the data were not reproducibly quantifiable. This was followed by an antiviral efficacy experiment in which mice infected with SARS-CoV-2 were orally dosed with 15 mg/kg Mpro61-HCl on a daily basis five times with the first dose starting at 10 h prior to infection, which displayed an encouraging delay in viral spread and disease progression (*SI Appendix, Fig. S3*). To build on these pilot experiments and increase the dosage of Mpro61-HCl, we turned to the use of gel capsules loaded with Mpro61-HCl, with which we were able to achieve a 100 mg/kg dose (*SI Appendix, Fig. S4A*). Infected mice dosed once daily using this capsule formulation continued to display an encouraging delay in viral spread and disease progression and had a significantly extended time to mortality (2 to 5 dpi compared to vehicle, *SI Appendix, Fig. S5*).

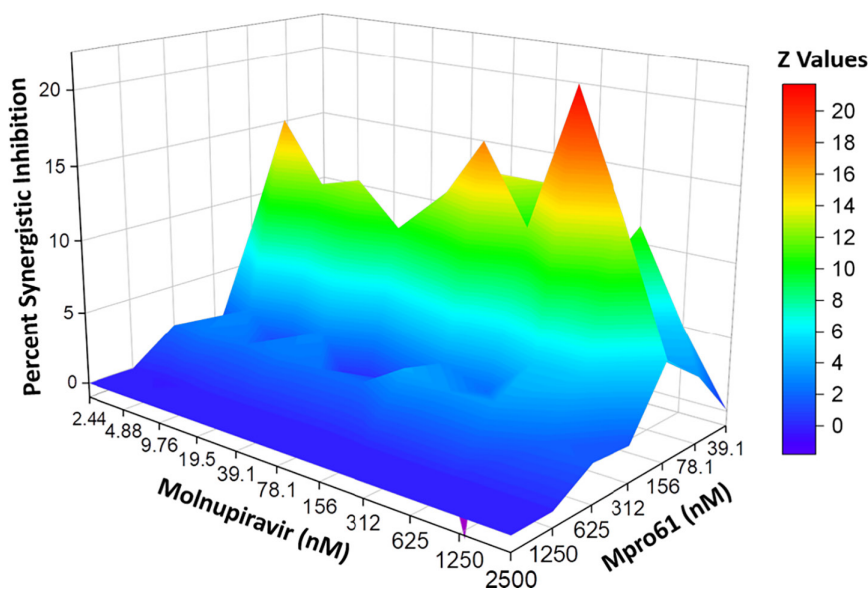


Fig. 4. Synergistic inhibition of SARS-CoV-2 replicon replication by combination of Mpro61 with molnupiravir, shown using MacSynergy II 3D plots. Peaks above the horizontal plane indicate synergistic inhibition. The results are from three experiments involving triplicate determination.

Pharmacological Studies. With this formulation showing promising results in mice, we maximized the amount of drug in each capsule to reach a 150 mg/kg dose and switched to a twice daily (BID) dosing regimen to improve upon PK and antiviral effects. Under these conditions, significant levels of Mpro61 could be detected as determined by Q-TOF-ESI-MS. As illustrated in Fig. 5 (*Left*), the serum concentration of Mpro61 ranged between 16 ng/mL and >500 ng/mL. Mpro61 levels in concentrated tissues displayed more consistent concentrations (Fig. 5, *Right*) with much higher levels in the lung (~2,000 ng/mL), liver (~1,000 ng/mL), kidney (~500 ng/mL), and gut (~1,000 ng/mL) compared to that in the brain (~16 ng/mL). Additional analysis of these samples by high-resolution mass spectrometry (HRMS) was carried out to determine the presence of various metabolites that might be anticipated, for instance, the N-demethylated uracil of Mpro61 or the benzylic ether cleavage as previously observed for similar Mpro analogs (28). There was no evidence for the N-demethylated uracil of Mpro61, however, a very small amount of the benzylic ether cleavage metabolite was observed as shown in *SI Appendix, Fig. S6*. In comparison with Mpro61, detection of this metabolite was significantly lower in the gut (19-fold), liver (86-fold), lung (313-fold), and kidney (856-fold), with no detection of this metabolite in the brain and serum. Encouraged by the detection of a significant amount of Mpro61 and little to no detection of metabolites in tissues, especially the brain and lung, the primary sites for SARS-CoV-2 infection in the B6-K18-hACE2 mouse model, a series of antiviral efficacy experiments were performed as described below.

In Vivo Efficacy and Synergy Studies. Efficacy and synergy studies were carried out in B6-K18-hACE2 mice infected with SARS-CoV-2 WA-1 nLuc virus (Fig. 6) as previously described (29, 30, 35). Mice were dosed twice daily with 150 mg/kg Mpro61-HCl ($n = 6$), 100 mg/kg molnupiravir ($n = 4$), or both compounds in combination ($n = 4$), with untreated vehicle-dosed mice as a control ($n = 4$). Molnupiravir was given for 3 d, while Mpro61-HCl was given for 7 d (Fig. 6*A*). Over the course of the experiment, bioluminescent imaging (BLI) was performed every other day to noninvasively quantify the presence of virus in the mice. Representative images show that while the virus spread rapidly in untreated mice, those dosed with either Mpro61-HCl or molnupiravir showed a delay in viral spread, and no luminescence was detected in mice dosed with both compounds in combination through 14 days postinfection (dpi) (Fig. 6*B–D*). Indeed, mice dosed with either Mpro61-HCl or molnupiravir showed a modest improvement in survival times, with one mouse dosed with

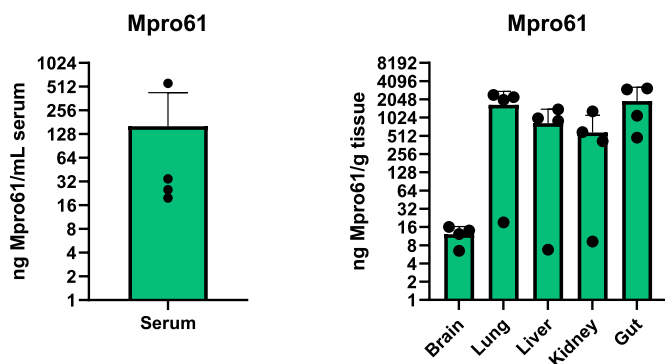


Fig. 5. Concentrations of Mpro61-HCl in the serum (*Left*) and various tissues (*Right*) of C57BL/6 mice. Mice were dosed with two 150 mg/kg capsules 10 to 12 h apart, and tissues were analyzed at 24 h by Q-TOF-ESI-MS. Mpro61-HCl concentrations were determined as described in the *Materials and Methods*.

Mpro61-HCl surviving until 14 dpi, seemingly making a full recovery. By comparison, all mice dosed with the combination of Mpro61-HCl and molnupiravir survived until 14 dpi, making a full recovery in body weight (Fig. 6*E* and *F*). This is demonstrated in the quantification of viral mRNA expression and viral titers within the mice; mice with a modest improvement in survival time display decreased viral mRNA and titers, while those which survived show no viral titers in all tissues at 14 dpi (Fig. 6*G* and *H*). These results were corroborated by the lack of flux in individual tissues as well, particularly the lung, brain, and nasal areas which are of particular interest, due to the respiratory and neuropathic effects of SARS-CoV-2 infection in this model (Fig. 7*A* and *B*). Additionally, cytokine mRNA expression was decreased in treated mice, with complete suppression of the pulmonary inflammatory response in mice dosed with the combination of Mpro61-HCl and molnupiravir (Fig. 7*C* and *D*). mRNA expression of Krt8, a marker for persistence of danger associated transitional progenitor cells derived from alveolar epithelial cells during healing/repair after lung injury, was also decreased in treated mice, with very little expression in mice treated with both Mpro61-HCl and molnupiravir, suggesting a significant decrease in lung damage due to viral infection (Fig. 7*E*). Taken together, these results support the potential of Mpro61-HCl as a M^{pro} inhibitor, both independently and particularly in combination with molnupiravir.

Discussion

The discovery and FDA approval of Paxlovid has been a significant step in the treatment of SARS-CoV-2 infection; however, the combination therapy is not a viable option for a significant number of patients due to its inclusion of a CYP450 metabolic inhibitor, ritonavir. While this metabolic inhibitor is required to prevent rapid degradation of the antiviral component targeting M^{pro} , nirmatrelvir, this CYP450 inhibition can precipitate drug–drug interactions in patients taking other medications due to accumulation of these medications in the body, leading to toxicity that prevents its safe use (23, 24). Among important criteria in our inhibitor design were compounds that would not inhibit CYP450 metabolism itself or require the addition of a metabolic inhibitor, providing a Paxlovid alternative for patients who require medication for other conditions, particularly immunocompromised patients who are additionally at higher risk for increased disease severity and SARS-CoV-2 infection.

Our effort to develop a class of M^{pro} inhibitors that avoided CYP450 inhibition utilized a computational and structural design strategy guided by FEP calculations starting from an initial virtual screening hit, the antiepileptic drug perampanel, as a starting scaffold, to using structure–activity relationships for enhancing binding interactions between the compound and the binding site, rapidly producing submicromolar inhibitors and an optimized lead compound, Mpro61, within a few dozen iterations of this process (Fig. 1).

Our initial computational model of perampanel binding suggested that the four-ring structure of this compound fit well within the S1' and S1 subsites of the M^{pro} active site, with the carbonyl group forming a hydrogen bond with the backbone of residue E166. Lead optimization efforts confirmed modeling predictions that rearrangement of the rings would allow for the formation of an additional hydrogen bond between the pyridine nitrogen and the sidechain nitrogen of conserved residue H163. Moreover, converting the cyanophenyl group to a uracil moiety extended this hydrogen bonding network, forming two hydrogen bonds with the backbone oxygen and nitrogen of residue T26, as well as one hydrogen bond with the backbone nitrogen of residue G143.

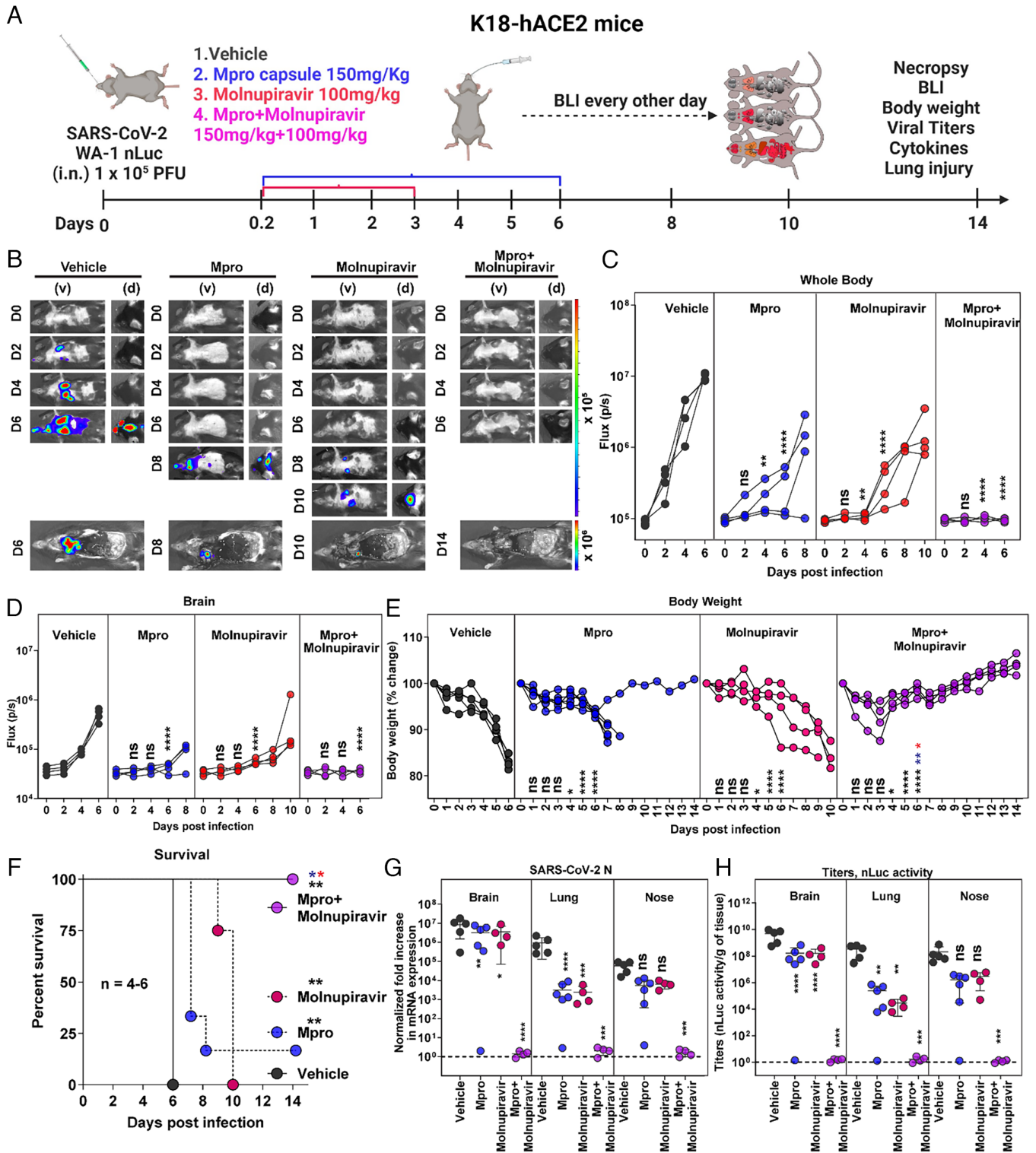


Fig. 6. Efficacy and synergy studies in K18-hACE2 mice infected with SARS-CoV-2 WA-1 nLuc virus. Mice were split into four groups for dosing: vehicle control ($n = 4$), twice daily 150 mg/kg Mpro61 ($n = 6$), twice daily 100 mg/kg molnupiravir ($n = 4$), and twice daily Mpro61 150 mg/kg in combination with molnupiravir 100 mg/kg ($n = 4$). Molnupiravir was given for 3 d, while Mpro61 was given for 6 d (A). Bioluminescent imaging of virus in mice, with images taken in the ventral (v) and dorsal (d) positions (B). Quantification of nLuc signal as flux (photons/sec) in the whole body (C) and brain (D). Changes in mouse body weight, with the initial body weight set as 100% (E). Kaplan-Meier survival curves of the mice in each dosing group ($n = 4$ to 6 per group) (F). Fold changes in viral mRNA expression (G) and viral loads (nLuc activity/mg tissue) (H) in the brain, lung, and nose of mice following death or 14 dpi (G). Grouped data in (C-E) and (G and H) were analyzed by two-way ANOVA followed by Tukey's multiple comparison tests. Statistical significance for group comparisons to vehicle is shown in black. $P < 0.05$; $**P < 0.01$; $***P < 0.001$; $****P < 0.0001$; ns not significant; mean values \pm SD are depicted.

Further modeling and computations targeted building into the S3 channel and S4 subsite to extend contacts with the active site, as this extension into the S3-S4 subsites has been previously associated with increased inhibition (14, 36). This likely occurs by

preventing substrates from binding within this region of the active site pocket and displacing the inhibitor. Structural and biochemical studies confirmed these predictions, with 3D protein-ligand structures, additionally showing the formation of another hydrogen

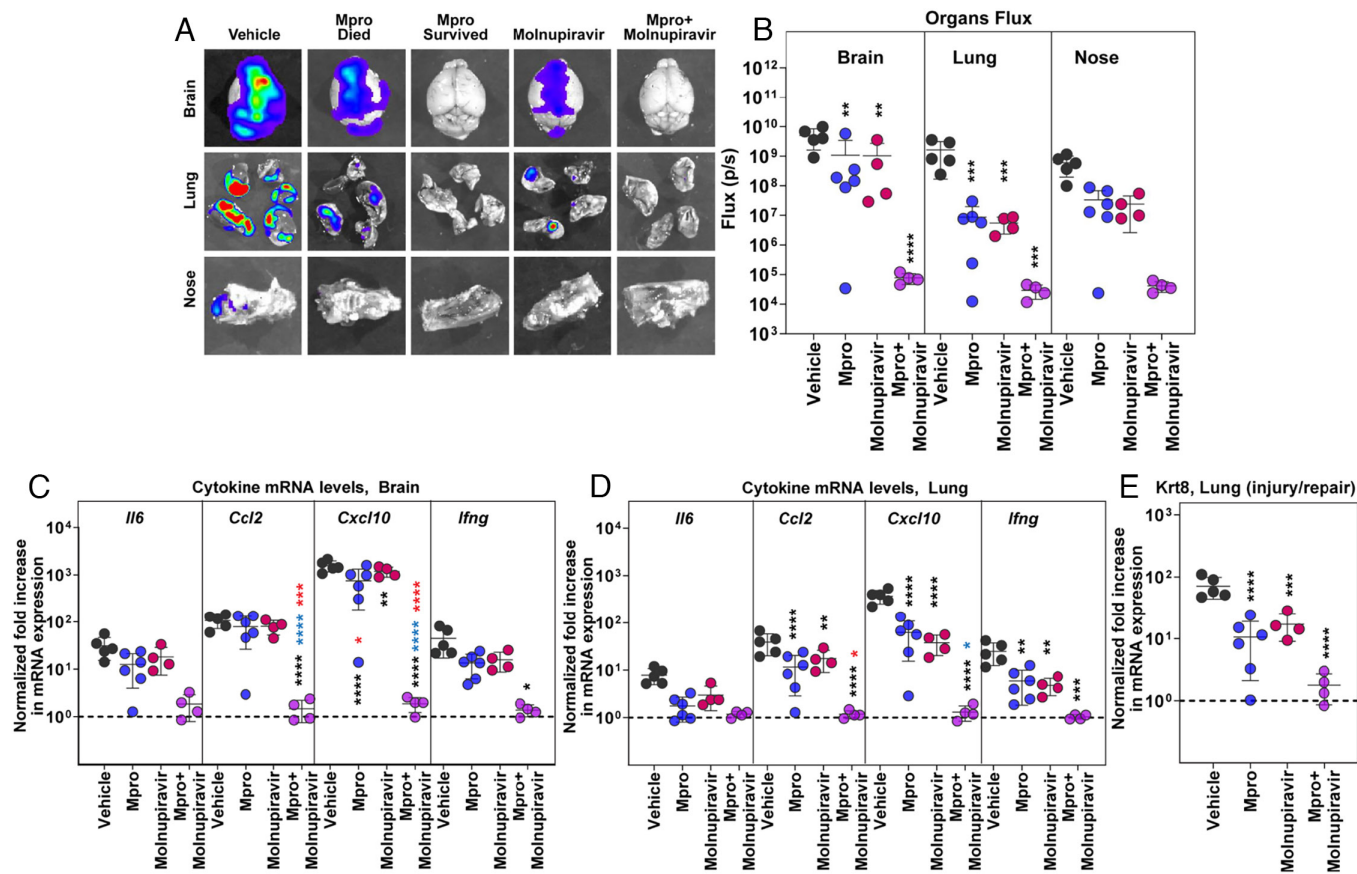


Fig. 7. Efficacy and synergy studies in B6-K18-hACE2 mice infected with SARS-CoV-2 WA-1 nLuc virus, as described in Fig. 6. Bioluminescent imaging of virus (A) and quantification of nLuc signal as flux (photons/sec) (B) in isolated tissues as indicated following necropsy at 14 dpi. Fold changes in cytokine mRNA expression in the brain (C) and lung (D) as well as mRNA expression of Krt8 in the lung (E) of mice following death or 14 dpi. Grouped data in (B–D) were analyzed by two-way ANOVA followed by Tukey's multiple comparison tests. The data in (E) were analyzed by one-way ANOVA followed by Tukey's multiple comparison tests. Statistical significance for group comparisons to vehicle is shown in black. * $P < 0.05$; ** $P < 0.01$; *** $P < 0.001$; **** $P < 0.0001$; ns not significant; mean values \pm SD are depicted.

bond between the oxygen of the added oxycyanophenyl group and the sidechain of conserved residue Q189, and biochemical assays revealing these modifications resulted in enhanced potency and the development of a submicromolar inhibitor. Cellular assays demonstrated that although these compounds were potent inhibitors biochemically, methylation of the uracil moiety was required for cell permeability for our optimized lead, Mpro61 (Fig. 2).

Notably, this method of binding is distinct from that of both currently available M^{pro} inhibitors, nirmatrelvir and ensitrelvir. Although ensitrelvir also binds M^{pro} noncovalently, it emphasizes interaction with the catalytic residue H41, disrupting activity. Although an extensive hydrogen bonding network is formed between ensitrelvir and the S1' and particularly the S1 subsites, ensitrelvir does not extend into the S3 and S4 subsites as Mpro61 does (PDB ID: 8HBK, *SI Appendix*, Fig. S2A) (14, 37). Nirmatrelvir, by contrast, binds covalently with the catalytic residue C145, and interactions with the active site are focused within the S1-S4 subsites, showing no extension into the S1' subsite (PDB ID: 8DZ2, *SI Appendix*, Fig. S2B) (38). As such, Mpro61 is distinct from these compounds in that it forms interactions spanning the M^{pro} active site.

With the 3D structures validating our structure–activity relationship modeling efforts, and previous biochemical and cellular assays supporting the potency of Mpro61 as an inhibitor and a lack of general cytotoxicity, it next was critical to perform in vitro pharmacological profiling to determine any potential off-target effects that would impact the activity of Mpro61 in vivo. In particular, we wanted to ensure that Mpro61 would not inhibit common CYP450 isoforms and avoid drug–drug interactions seen with Paxlovid

offering a potential alternative for patients whose therapeutic regimens would render them susceptible to these interactions. In vitro pharmacological profiling with a panel containing common CYP450 isoforms revealed no significant inhibition by Mpro61, highlighting this feature as a potential advantage over Paxlovid, and supporting further preclinical development of Mpro61 as a possible alternative. Additionally, other ion channels and receptors examined in the profiling panel showed no significant off-target effects except for slight inhibition of the hERG ion channel at high concentrations, lending further support for continued evaluation (Fig. 3).

While previous cellular assays showed the potency of Mpro61 in cells as an individual direct-acting antivirals (DAA), we were additionally interested in the potential of Mpro61 to act synergistically with other SARS-CoV-2 inhibitors. Synergy with molnupiravir, an FDA-approved RdRp inhibitor, was of particular interest due to its status as a previously approved drug, its lack of CYP450 inhibition or need to be dosed alongside a CYP450 inhibitor, and its antiviral activity targeting a step in viral replication and enzyme distinct from that of Mpro61 (39, 40). Cellular assays examining potential synergy between Mpro61 and molnupiravir revealed a strong increase in percent inhibition at low concentrations of both compounds, displaying potent synergy (Fig. 4). Taken together, these studies warranted further evaluation in proof of concept in vivo studies to examine the potential of Mpro61 not only as an individual DAA but also as a component in a combination therapy with molnupiravir.

With multiple animal models for SARS-CoV-2 in vivo studies available, we chose the B6-K18-hACE2 mouse model as it allows

for infection with native SARS-CoV-2 and displays aggressive disease symptoms and progression of virus, more closely mimicking the more aggressive COVID cases that would be seen in susceptible immunocompromised patients (29). A strain of SARS-CoV-2 additionally encoding a nLuc reporter was used for infection, allowing for noninvasive detection of virus through BLI and visualization of viral spread through the mouse over time (29). In developing a suitable formulation for in vivo dosing, conversion of Mpro61 to a hydrochloride salt form (Mpro61-HCl) moderately improved solubility, allowing for the preparation of a 15 mg/kg dose in suspension with 5% Tween 80 in phosphate-buffered saline that could be administered via oral gavage. At this dose, encouraging results were obtained, showing that viral spread was slightly delayed; however, it was clear that a higher dose was necessary to properly determine the efficacy of Mpro61-HCl in mice (*SI Appendix, Fig. S3*). Due to constraints with low solubility of Mpro61-HCl, we sought out an alternative delivery method that would allow effective oral dosing as a key criterion. Although uncommon, loaded gel capsules have been previously used with success in studies with rats and larger mice (41, 42). These capsules would allow for oral administration of a much higher dose, increasing the amount of drug circulating in the mice and improving our ability to determine the pharmacological properties and efficacy of Mpro61-HCl in mice. Indeed, initial capsule dosing experiments utilizing a 100 mg/kg dose show improved efficacy over the 15 mg/kg dose, with a promising increase in delay of viral spread and disease progression (*SI Appendix, Fig. S5*). To further maximize the dosing and the amount of drug circulating within the mice, we increased the dose of Mpro61-HCl per capsule to 150 mg/kg, with capsules administered twice daily (BID) to increase and maintain drug levels in the serum and tissues.

Using this final dosing regimen, we performed a 24 h PK experiment with BID dosing (2 × 150 mg/kg), quantifying levels of Mpro61-HCl in the serum, brain, lung, liver, kidney, and gut of euthanized mice. Previous studies have shown uncoated capsules to begin dissolving in the stomach after approximately 15 min, with the capsule entirely dissolved within 1 h (42). As the capsule dissolves, the compound in these studies was rapidly absorbed by the stomach and into the plasma, with a peak concentration of the compound in the plasma occurring during capsule dissolution (42). Although drug concentration in the serum appeared lower in most mice at 24 h, significant concentrations of Mpro61-HCl were observed in the brain and lung. As a point of reference, the levels of Mpro61-HCl in the brain were comparable to those seen in a similar study where mice were dosed twice daily with 600 mg/kg nirmatrelvir, and the concentration of Mpro61-HCl in the lung was nearly 10-fold higher than the concentration of nirmatrelvir (Fig. 5) (30). Notably, the dosage of Mpro61-HCl used in these experiments is fourfold lower than that used when dosing with nirmatrelvir, making the detection of comparable or higher levels of drug in the tested organ tissues particularly encouraging. Moreover, our evaluation of possible metabolites using HRMS for in vivo PK, including cleavage of the benzylic ether or N-demethylation, did not reveal significant metabolism of Mpro61 and confirmed high levels of the compound in target lung and brain tissues (*SI Appendix, Fig. S6*). (28) In addition, as SARS-CoV-2 is a respiratory infection with known neuropathic effects, the presence of significant levels of Mpro61-HCl in the lung and brain was a promising benchmark when moving forward with efficacy and synergy experiments in mice, even at this relatively low dose.

As with our earlier cellular assays, we performed in vivo efficacy testing of Mpro61-HCl both as a single antiviral agent and in synergistic combination with molnupiravir. While mice given molnupiravir alone showed a modest improvement in disease progression over the control cohort, all mice still succumbed to

infection. Although most mice dosed with Mpro61-HCl alone showed only a slight improvement in disease progression, one mouse fully recovered from infection. This result is encouraging given the fourfold lower dose than is used when dosing with nirmatrelvir, and it is possible that higher doses of Mpro61-HCl could provide more complete antiviral protection. Even more encouragingly, all mice dosed with Mpro61-HCl in combination with molnupiravir made a full recovery (Figs. 6 and 7).

Taken together, these proof-of-concept studies present Mpro61-HCl as a viable SARS-CoV-2M^{pro} inhibitor. As it does not inhibit CYP450 metabolism or require dosing with a metabolic inhibitor, as is the case with nirmatrelvir, it has decreased potential for negative drug–drug interactions and toxicity and additionally does not show any other significant off-target effects. Even at a much lower dose than nirmatrelvir, we see significant concentrations of Mpro61-HCl in the serum and in multiple organs, including the particularly relevant lung and brain tissues. The in vivo experiments in this study confirm that Mpro61-HCl has antiviral potential individually and demonstrate robust protection against infection when given in combination with molnupiravir. Additionally, preliminary biochemical assays demonstrate that Mpro61 maintains antiviral activity against SARS-CoV-1M^{pro}, suggesting that it may also be useful against other members of this coronavirus family. These qualities establish Mpro61-HCl as a promising preclinical candidate and warrant further study of it as a potential alternative to Paxlovid.

Materials and Methods

Chemical and Compound Synthesis. Compounds Mpro48, Mpro57, and Mpro61 were synthesized as previously described (13, 14). A commercial source for Mpro61 as the free base form from Tocris Bioscience is now available (43). As noted, it was necessary to prepare the hydrochloride salt of Mpro61 for the PK and in vivo studies. The synthetic details for the Mpro61-HCl salt are provided in *SI Appendix*. The large-scale synthesis of Mpro61HCl salt for animal studies was carried out by the WuXi AppTec chemistry team at WuXi Inc. The molnupiravir (also called EIDD1931) was purchased from MedChemExpress, Monmouth, NJ. All MS analysis utilized LC-MS-grade solvents that were obtained from Fisher Scientific.

Formulation of Mpro61 in Gel Capsules. The gelatin capsules (Size M) and capsule filler assembly obtained from Torpac (NJ, USA) were used for loading the drug Mpro61. An illustration of this process is summarized in *SI Appendix, Fig. S3*. The process involved several steps for filling these capsules. Initially, each capsule was weighed before drug filling using a precision weighing machine. Subsequently, a single capsule was isolated and its body was securely placed in a designated holder. A funnel was positioned over the capsule body within the holder to facilitate precise dosing. The drug, in powdered form, was carefully dosed into the capsule through the funnel. Once the required drug quantity was filled into the funnel, a tamper was used to compress the filling material, ensuring a proper fit within the capsule body. Afterward, the funnel was gently removed. The capsule's cap was then placed onto the body, firmly pressed to lock them together. The filled capsule was removed from the holder. To determine the drug quantity in each capsule, we measured the weight of the filled and closed capsules and then subtracted this from the weight of an empty capsule.

Crystallography of Mpro61-Bound M^{pro} Complexes. Recombinant SARS-CoV-2M^{pro} was expressed using plasmid generously donated by Zhang et al. and purified as described previously (7). M^{pro} protein samples at 25 mg/mL were thawed on ice and incubated at 37 °C with 5% 13.3 mM Mpro61 in DMSO for 90 min. Samples were then centrifuged at 12,800 × g for 25 min at room temperature, and the supernatant was used to set up crystallization screens. The commercially available PEGRx1 and PEGRx2 screening conditions (Hampton Research) were used, with wells containing 80 μL of reservoir solution. Trays were set up manually with 2 μL drops in a 1:1 protein/reservoir solution ratio and utilizing the sitting-drop vapor-diffusion method at 16 °C. Stacked plate crystals grew over 48 h and were harvested, cryoprotected with 15% glycerol and 5% 13.3 mM Mpro61 in DMSO, and flash frozen in liquid nitrogen. X-ray data were collected at the Argonne National

Laboratory (APS NE-CAT 24-ID-E) and underwent phasing using XDS. Molecular replacement was performed using PDB ID: 6Y2G as the search model. Phenix was used for successive rounds of refinement and COOT was used for model building.

Replicon Synergy Assays Assessing Inhibition of Viral Replication. As described previously, a SARS-CoV-2 replicon was generated by replacing the Spike gene with a Nano luciferase (Nluc) gene within a full-length infectious cDNA clone of the viral genome stably maintained within the yeast artificial chromosome (YAC) pCC1BAC-HIS3/SARS-CoV-2 (14, 32, 44). Briefly, the Nluc gene was amplified to add flanking SARS-CoV-2 sequences and remove an internal EagI site in two steps. First, the 5' end of the Nluc gene was amplified by using Q5 DNA polymerase (New England Biolabs) with primers YO-3778 (5'-GAG TTG TTATTT CTA GTG ATG TTC TTG TTA ACA ACT AAA CGA ACA ATG GTC TTC ACA CTC GAA GAT TT-3') and YO-4096 (5'-GCC TTC ATA GGG GCG TCC GAA ATA GTC GAT-3'); the 3' end of the Nluc gene was amplified by using Q5 DNA polymerase with primers YO-4101 (5'-CGA CTA TTT CGG ACG CCC CTA TGA AGG CAT CGC CGT GTT-3') and YO-3779 (5'-CAG TTC CAA TTG TGA AGA TTC TCA TAA ACA AAT CCA TAA GTT CGT TTA CGC CAG AAT GCG TTC GCA CA-3'). The full-length Nluc gene was then amplified by using Q5 DNA polymerase with primers YO-3778 and YO-3779 and inserted into BamHI-linearized pCC1BAC-HIS3/SARS-CoV-2 by cotransfection into yeast VL6-48N (45) and selection of homologous recombinants on histidine-deficient media. YACs were recovered from liquid cultures by treatment with zymolase (Zymo Research) and ZymoPURE plasmid midiprep kits (Zymo Research), then transformed into Epi300 bacterial cells (Lucigen). Chloramphenicol-resistant colonies were picked and grown in liquid media with CopyControl induction solution, then used to prepare amplified YAC by using the ZymoPURE plasmid midiprep kit. The replicon-bearing YAC was sequence verified by whole plasmid sequencing (Massachusetts General Hospital Genome DNA Core) and linearized by overnight digestion with EagI. Linearized transcription templates were purified by treatment at 55 °C with 0.5% (W/V) SDS and 3 units proteinase K followed by two rounds of phenol/chloroform extraction and ethanol precipitation. Replicon RNAs were transcribed from purified transcription templates with the T7 Ribomax kit (Promega) and anti-reverse cap analog (New England Biolabs). RNAs were purified by treatment with RQ1 DNase (Promega) and RNA Clean & Concentrator-25 kit (Zymo), eluted into 2 mM sodium citrate (pH 6.4), aliquoted in 1 µg portions, and stored frozen at -80 °C. RNAs were transfected into BHK cells engineered to express a human codon-optimized SARS-CoV-2 nucleoprotein gene by electroporation (46). Cells were then seeded in multiple replicates on 96-well plates containing serial dilutions of Mpro61 and molnupiravir. The following day, Nluc activity was measured by using NanoGlo reagents (Promega) with a CentroXS3 LB 960 microplate luminometer (Berthold).

Experiments in B6-K18-hACE2 Mice. hACE2 transgenic B6 mice (heterozygous) were obtained from Jackson Laboratory. Six- to eight-week-old male and female mice were used for all experiments, which were conducted as previously described (29, 30). The heterozygous mice were crossed and genotyped to select heterozygous mice for experiments by using the primer sets recommended by Jackson Laboratory. All studies described here were approved by Institutional Animal Care and Use Committees as well as SOPs approved by the Institutional Environmental Health and Biosafety committee. All animals were maintained in the (SPF-free) barrier facility of the Yale University Animal Resource Centre (YARC) within a 14:10 light: dark cycle. All SARS-CoV-2-infected animals were housed under BSL3 containment. Each cohort size was $n = 4$ to 6 to allow statistical testing and conducted as 2 to 3 biological replicates ($n = 2$ to 3 per replicate) to allow parallel evaluation of different cohorts based on a prior power analysis from pilot experiments and previous studies. Animals with sex- and age-matched littermates were included randomly in the experiments. At the time of experimentation, care was taken to include equal numbers of male and female mice whenever possible to ensure that the sex of the animals does not constitute a biological variable during analysis.

SARS-CoV-2 Infection and Treatment Conditions. For in vivo experiments, 6- to 8-wk-old male and female mice were intranasally challenged with 1×10^5 PFU SARS-CoV-2-nLuc (strain 2019-nCoV/USA_WA1/2020) in 25 to 30 µL volume under anesthesia similar to studies previously described (29, 30, 35) (0.5 to 5% isoflurane delivered using precision Dräger vaporizer with oxygen flow rate of 1 L/min). The starting body weight was set to 100%. For survival experiments, mice were monitored every 8 to 12 h starting 6 d after virus challenge. Lethargic and moribund mice or mice that had lost more than 20% of their body weight were euthanized by CO₂ using AVMA guidelines and considered to have succumbed to

infection for Kaplan–Meier survival plots. Mice were considered to have recovered if they gained back all the lost weight. Mpro61 was prepared at 15 mg/kg as suspension (5% Tween 80 in phosphate-buffered saline) and 100 mg/kg doses in a capsule formulation. The drug was suspended in this solution by sonicating for 5 min and heating to 42 °C. Mpro61 solution was prepared fresh daily in a volume of 500 µL and administered orally using an oral gavage needle once daily. Mpro61 150 mg/kg doses were prepared by loading drug (see above) into gelatin capsules (Torpac, size M) and administered twice daily (BID) (total dose of 300 mg/kg per day) at 10 to 12 h intervals until 6 dpi. Molnupiravir was dissolved in a solution of 10% PEG400 and 2.5% Kolliphor-EL (Vehicle) in sterile milli-Q water by shaking in a thermomixer for 15 min and then by vortexing for 5 min. Molnupiravir solution was prepared fresh daily. Molnupiravir (100 mg/kg body weight) was made in a volume of 150 µL and administered orally using an oral gavage needle (20 gauge) starting at 8 hpi. On the following days, 100 mg/kg body weight of molnupiravir was administered twice daily (BID, 10 to 12 h apart) until 3 dpi (total dose of 200 mg/kg per day) for all experiments designed to test synergy with Mpro61.

PK Experiments–Dosing, Drug Extraction, and Preparation of PK Samples for MS Analysis. A cohort of four mice were given two doses of 150 mg/kg Mpro61 10 to 12 h apart and euthanized by CO₂ exposure 24 h after the first dose was administered. Whole blood and tissue samples (brain, lung, liver, kidney, and gut) were collected. Whole blood samples were allowed to clot by leaving at room temperature for 4 h, then centrifuged at $6,000 \times g$ for 15 min at room temperature to collect the serum. Mpro61 was extracted from serum using MTBE extraction. 800 µL 0.1 M NaOH and 1.4 mL MTBE were added to 300 µL of each serum sample. Samples were then shaken for 15 min and briefly vortexed, then centrifuged at $16,000 \times g$ for 10 min at 4 °C. The organic layer was removed and dried using a SpeedVac (Savant). This extraction was repeated twice, with the final extraction left shaking for 18 h. Tissue samples were weighed and manually homogenized in 0.5 mL milliQ water per 200 mg tissue. Following homogenization, 2.5 mL acetonitrile per 200 mg tissue was added. Samples were then shaken for 15 min and briefly vortexed, then centrifuged at $5,000 \times g$ for 20 min at 4 °C. The supernatant was removed and dried using a GeneVac. Once dried, 1 mL acetonitrile was added and samples were sonicated for 10 min, then centrifuged at $16,000 \times g$ for 10 min at 4 °C. The supernatant was removed and dried using a SpeedVac (Savant).

Q-TOF-MS Analysis of PK Samples. Mpro61 was extracted from serum and tissue samples as described above. Additional samples were prepared for determination of two standard curves, with Mpro61 in acetonitrile and Mpro61 extracted from mouse serum controls. Dried drug extraction samples were reconstituted in 30 µL acetonitrile, then sonicated for 10 min, vortexed briefly, and centrifuged at $13,000 \times g$ for 10 min at room temperature. 10 µL of each sample was analyzed by LC-MS as described below. Serum extraction efficiency (19%) was determined through comparison of the Mpro61 in acetonitrile and Mpro61 extracted from mouse serum standard curves. The concentration of Mpro61 in serum samples was determined through comparison to the serum extracted standard curve, then corrected using the average serum extraction efficiency. The concentration of Mpro61 in tissue samples was determined through comparison to the acetonitrile standard curve.

Quantitation of Mpro61 in serum or tissues was carried out using high-performance liquid chromatography high-resolution electrospray ionization mass spectrometry (HPLC-ESI-MS) data for analysis. This involved using an Agilent iFunnel 6550 quadrupole time-of-flight mass spec (Q-TOF-MS) instrument fitted with an ESI source coupled to an Agilent 1290 Infinity HPLC system and a Phenomenex Luna C18 (2) (100 Å) 10 µm column (10.0 × 250 mm²) (Phenomenex) with a water: acetonitrile gradient containing 0.1% formic acid at 0.7 mL/min: 0 to 30 min, 10 to 100% acetonitrile.

Data, Materials, and Software Availability. Protein crystal structure data have been deposited in Protein Databank (PDB ID: 8UR9) (47). All other data are included in the manuscript and/or *SI Appendix*.

ACKNOWLEDGMENTS. Funding of this work was provided by NIH GM032136 to W.L.J., NIH R24OD026440 to P.K., Yale CoReCT pilot funding for COVID to W.L.J. and K.S.A., NIH/NIAID 1U19AI171443 (K.S.A., Developmental Project), and T32 GM148333 to C.P. This research used resources AMX (Highly Automated Macromolecular Crystallography) and FMX (Frontier Microfocusing Macromolecular Crystallography) of the National Synchrotron Light Source II, a U.S. Department of Energy (DOE) Office of Science User Facility operated for the DOE Office of

Science by Brookhaven National Laboratory under Contract No. DE-SC0012704. The Center for BioMolecular Structure is primarily supported by the NIH, National Institute of General Medical Sciences (NIGMS) through a Center Core P30 Grant (P30GM133893), and by the DOE Office of Biological and Environmental Research (KP1605010). This work is also based upon research conducted at the Northeastern Collaborative Access Team beamlines, which are funded by the NIGMS from the NIH (P30 GM124165). The Eiger 16M detector on 24-ID-E is funded by an NIH-ORIP HEI grant (S100D021527). This research used resources of the Advanced Photon Source, a U.S. DOE Office of Science User Facility operated for the DOE Office of Science by Argonne National Laboratory under Contract No. DE-AC02-06CH11357.

Author affiliations: *Department of Pharmacology, Yale University School of Medicine, New Haven, CT 06520-8066; †Department of Internal Medicine, Section of Infectious Diseases, Yale University School of Medicine, New Haven, CT 06520-8066; ‡Department of Microbiology, Immunology and Genetics Graduate School for Biomedical Sciences, University of North Texas Health Science Center, Fort Worth, TX 76107; ††Department of Microbial Pathogenesis, Yale University School of Medicine, New Haven, CT 06520-8066; †††Department of Chemistry, Yale University, New Haven, CT 06520-8107; and ††††Department of Molecular Biophysics and Biochemistry, Yale University School of Medicine, New Haven, CT 06520-8066

Author contributions: A.P.R., W.M., J.M.C., B.D.L., P.K., W.L.J., and K.S.A. designed research; C.P., I.U., A.P.R., S.Z., Q.W., K.A.S., C.Z., W.M., B.D.L., P.D.U., P.K., and K.S.A. performed research; C.P., I.U., A.P.R., S.Z., Q.W., K.A.S., W.M., J.M.C., B.D.L., P.D.U., P.K., and K.S.A. analyzed data; and C.P., I.U., A.P.R., W.M., J.M.C., P.K., W.L.J., and K.S.A. wrote the paper.

1. A. A. Rabaan *et al.*, An updated review on pathogenic coronaviruses (CoVs) amid the emergence of SARS-CoV-2 variants: A look into the repercussions and possible solutions. *J. Infect. Public Health* **16**, 1870–1883 (2023), 10.1016/j.jiph.2023.09.004.
2. Centers for Disease Control and Prevention, COVID data tracker. <https://covid.cdc.gov/covid-data-tracker/#data-tracker-home> (2023). Accessed 27 October 2023.
3. Centers for Disease Control and Prevention, SARS-CoV-2 variant classifications and definitions. <https://www.cdc.gov/coronavirus/2019-ncov/variants/variant-classifications.html> (2023). Accessed 27 October 2023.
4. Z. Jin *et al.*, Structure of M(pro) from SARS-CoV-2 and discovery of its inhibitors. *Nature* **582**, 289–293 (2020), 10.1038/s41586-020-2223-y.
5. T. Pillaiyar, M. Manickam, V. Namasivayam, Y. Hayashi, S.-H. Jung, An overview of severe acute respiratory syndrome-coronavirus (SARS-CoV) 3CL protease inhibitors: Peptidomimetics and small molecule chemotherapy. *J. Med. Chem.* **59**, 6595–6628 (2016), 10.1021/acs.jmedchem.5b01461.
6. A. K. Ghosh, M. Brindisi, D. Shahabi, M. E. Chapman, A. D. Mesecar, Drug development and medicinal chemistry efforts toward SARS-coronavirus and Covid-19 therapeutics. *ChemMedChem* **15**, 907–932 (2020), 10.1002/cmdc.202000223.
7. L. Zhang *et al.*, Crystal structure of SARS-CoV-2 main protease provides a basis for design of improved alpha-ketoamide inhibitors. *Science* **368**, 409–412 (2020), 10.1126/science.abb3405.
8. Z. Jin *et al.*, Structural basis for the inhibition of SARS-CoV-2 main protease by antineoplastic drug carmofur. *Nat. Struct. Mol. Biol.* **27**, 529–532 (2020), 10.1038/s41594-020-0440-6.
9. A. Gimeno *et al.*, Prediction of novel inhibitors of the main protease (M-pro) of SARS-CoV-2 through consensus docking and drug reposition. *Int. J. Mol. Sci.* **21**, 3793 (2020), 10.3390/ijms21113793.
10. C. Ma *et al.*, Boceprevir, GC-376, and calpain inhibitors II, XII inhibit SARS-CoV-2 viral replication by targeting the viral main protease. *Cell Res.* **30**, 678–692 (2020), 10.1038/s41422-020-0356-z.
11. W. Dai *et al.*, Structure-based design of antiviral drug candidates targeting the SARS-CoV-2 main protease. *Science* **368**, 1331–1335 (2020), 10.1126/science.abb4489.
12. M. M. Ghahremanpour *et al.*, Identification of 14 known drugs as inhibitors of the main protease of SARS-CoV-2. *ACS Med. Chem. Lett.* **11**, 2526–2533 (2020), 10.1021/acsmchemlett.0c00521.
13. C. H. Zhang *et al.*, Potent noncovalent inhibitors of the main protease of SARS-CoV-2 by molecular sculpting of the drug perampanel guided by free energy perturbation calculations. *ACS Cent. Sci.* **7**, 467–475 (2021), 10.1021/acscentsci.1c00309.
14. C. H. Zhang *et al.*, Optimization of triarylpyridinone inhibitors of the main protease of SARS-CoV-2 to low-nanomolar antiviral potency. *ACS Med. Chem. Lett.* **12**, 1325–1332 (2021), 10.1021/acsmchemlett.1c00326.
15. US Food and Drug Administration, Coronavirus (COVID-19) update: FDA authorizes first oral antiviral for treatment of COVID-19. <https://www.fda.gov/news-events/press-announcements/coronavirus-covid-19-update-fda-authorizes-first-oral-antiviral-treatment-covid-19> (2021). Accessed 27 October 2023.
16. R. E. Cavazzoni, RE: Emergency use authorization 105. <https://www.fda.gov/media/155049/download> (2023). Accessed 27 October 2023.
17. Pfizer Inc, Paxlovid (nirmatrelvir/ritonavir). Package insert: https://www.accessdata.fda.gov/drugsatfda_docs/label/2023/217188s0001bl.pdf. Accessed 27 October 2023.
18. AbbVie, Norvir (ritonavir). Package insert: https://www.accessdata.fda.gov/drugsatfda_docs/label/2017/2095121bl.pdf. Accessed 27 October 2023.
19. I. F. Sevrioukova, T. L. Poulos, Structure and mechanism of the complex between cytochrome P4503A4 and ritonavir. *Proc. Natl. Acad. Sci. U.S.A.* **107**, 18422–18427 (2010), 10.1073/pnas.1010693107.
20. L. Profit, V. A. Eagling, D. J. Back, Modulation of P-glycoprotein function in human lymphocytes and Caco-2 cell monolayers by HIV-1 protease inhibitors. *AIDS* **13**, 1623–1627 (1999), 10.1097/00002030-199909100-00004.
21. R. L. Atmar, N. Finch, New perspectives on antimicrobial agents: Molnupiravir and nirmatrelvir/ritonavir for treatment of COVID-19. *Antimicrob. Agents Chemother.* **66**, e0240421 (2022), 10.1128/aac.02404-21.
22. J. Gerhart *et al.*, Real-world evidence of the top 100 prescribed drugs in the USA and their potential for drug interactions with nirmatrelvir; ritonavir. *AAPS J.* **25**, 73 (2023), 10.1208/s12248-023-00832-3.
23. A. Shah, A. Nasrullah, M. Ali Butt, M. Young, Paxlovid with caution: Novel case of Paxlovid-induced tacrolimus toxicity in a cardiac transplant patient. *Eur. J. Case Rep. Intern. Med.* **9**, 003528 (2022), 10.12890/2022_003528.
24. C. Young, T. Papiro, J. H. Greenberg, Elevated tacrolimus levels after treatment with nirmatrelvir/ritonavir (Paxlovid) for COVID-19 infection in a child with a kidney transplant. *Pediatr. Nephrol.* **38**, 1387–1388 (2023), 10.1007/s00467-022-05712-0.
25. A. K. Singh, A. Singh, R. Singh, A. Misra, An updated practical guideline on use of molnupiravir and comparision with agents having emergency use authorization for treatment of COVID-19. *Diabetes Metab. Syndr.* **16**, 102396 (2022), 10.1016/j.dsx.2022.102396.
26. R. Shimizu *et al.*, Evaluation of the drug-drug interaction potential of ensitrelvir fumaric acid with cytochrome P450 3A substrates in healthy Japanese adults. *Clin. Drug. Investig.* **43**, 335–346 (2023), 10.1007/s40261-023-01265-8.
27. H. Mukae *et al.*, Efficacy and safety of ensitrelvir in patients with mild-to-moderate Coronavirus disease 2019: The phase 2b part of a randomized, placebo-controlled, phase 2/3 study. *Clin. Infect. Dis.* **76**, 1403–1411 (2023), 10.1093/cid/ciac933.
28. I. Jacobs *et al.*, Design and optimization of novel competitive, non-peptidic, SARS-CoV-2 M(pro) inhibitors. *ACS Med. Chem. Lett.* **14**, 1434–1440 (2023), 10.1021/acsmchemlett.3c00335.
29. I. Ullah *et al.*, Live imaging of SARS-CoV-2 infection in mice reveals that neutralizing antibodies require Fc function for optimal efficacy. *Immunity* **54**, 2143–2158.e15 (2021), 10.1016/j.immuni.2021.08.015.
30. I. Ullah *et al.*, Combinatorial regimens augment drug monotherapy for SARS-CoV-2 clearance in mice. [bioRxiv \[Preprint\] \(2023\)](https://doi.org/10.1101/2023.05.31.543159). <https://doi.org/10.1101/2023.05.31.543159>.
31. Z. A. Shyr, Y.-S. Cheng, D. C. Lo, W. Zheng, Drug combination therapy for emerging viral diseases. *Drug Discov. Today* **26**, 2367–2376 (2021), 10.1016/j.drudis.2021.05.008.
32. T. Thi Nhu Thao *et al.*, Rapid reconstruction of SARS-CoV-2 using a synthetic genomics platform. *Nature* **582**, 561–565 (2020), 10.1038/s41586-020-2294-9.
33. M. N. Prichard, C. Shipman Jr., A three-dimensional model to analyze drug-drug interactions. *Antiviral Res.* **14**, 181–205 (1990).
34. W. Dong *et al.*, The K18-human ACE2 transgenic mouse model recapitulates non-severe and severe COVID-19 in response to an infectious dose of the SARS-CoV-2 virus. *J. Virol.* **96**, e0096421 (2022), 10.1128/JVI.00964-21.
35. I. Ullah *et al.*, Bioluminescence imaging reveals enhanced SARS-CoV-2 clearance in mice with combinatorial regimens. *iScience* **27**, 109049 (2024), 10.1016/j.isci.2024.109049.
36. M. G. Deshmukh *et al.*, Structure-guided design of a perampanel-derived pharmacophore targeting the SARS-CoV-2 main protease. *Structure* **29**, 823–833.e5 (2021), 10.1016/j.str.2021.06.002.
37. Y. Duan *et al.*, Molecular mechanisms of SARS-CoV-2 resistance to nirmatrelvir. *Nature* **622**, 376–382 (2023), 10.1038/s41586-023-06609-0.
38. G. D. Noske *et al.*, Structural basis of nirmatrelvir and ensitrelvir activity against naturally occurring polymorphisms of the SARS-CoV-2 main protease. *J. Biol. Chem.* **299**, 103004 (2023), 10.1016/j.jbc.2023.103004.
39. Merck, Lagevrio (molnupiravir). Package insert: <https://www.merck.com/eua/molnupiravir-hcp-fact-sheet.pdf>. Accessed 27 October 2023.
40. B. Dave *et al.*, Molnupiravir: An antiviral drug against COVID-19. *Arch. Virol.* **168**, 252 (2023), 10.1007/s00705-023-05881-9.
41. N. G. Lamson *et al.*, The strawberry-derived permeation enhancer pelargonidin enables oral protein delivery. *Proc. Natl. Acad. Sci. U.S.A.* **119**, e2207829119 (2022), 10.1073/pnas.2207829119.
42. N. Reix *et al.*, Duodenum-specific drug delivery: In vivo assessment of a pharmaceutically developed enteric-coated capsule for a broad applicability in rat studies. *Int. J. Pharm.* **422**, 338–340 (2012), 10.1016/j.ijpharm.2011.10.017.
43. A. Moloney, H. J. Maple, Developing, choosing, and using the chemical toolbox for infectious diseases research. *ACS Infect. Dis.* **9**, 2–4 (2023), 10.1021/acscinfdis.2c00539.
44. B. D. Lindenbach, Reinventing positive-strand RNA virus reverse genetics. *Adv. Virus Res.* **112**, 1–29 (2022), 10.1016/bs.avir.2022.03.001.
45. V. Lariouon, N. Kouprina, G. Solomon, J. C. Barrett, M. A. Resnick, Direct isolation of human BRCA2 gene by transformation-associated recombination in yeast. *Proc. Natl. Acad. Sci. U.S.A.* **94**, 7384–7387 (1997), 10.1073/pnas.94.14.7384.
46. B. D. Lindenbach, C. M. Rice, Trans-complementation of yellow fever virus NS1 reveals a role in early RNA replication. *J. Virol.* **71**, 9608–9617 (1997), 10.1128/JVI.71.12.9608-9617.1997.
47. C. Papini, C. H. Zhang, W. L. Jorgensen, K. S. Anderson, Crystal structure of the SARS-CoV-2 main protease in complex with compound 61. PDB. <https://www.rcsb.org/structure/unreleased/8UR9>. Deposited 2 November 2023.